ACS APPLIED MATERIALS & INTERFACES

Research Article

www.acsami.org

Multiferroic Behavior of Templated $BiFeO_3$–$CoFe_2O_4$ Self-Assembled Nanocomposites

Nicolas M. Aimon,* Dong Hun Kim, XueYin Sun, and C. A. Ross*

Department of Materials Science and Engineering, Massachusetts Institute of Technology, Cambridge, Massachusetts 02139, United States

Supporting Information

ABSTRACT: Self-assembled $BiFeO_3$–$CoFe_2O_4$ nanocomposites were templated into ordered structures in which the ferrimagnetic $CoFe_2O_4$ pillars form square arrays of periods 60–100 nm in a ferroelectric $BiFeO_3$ matrix. The ferroelectricity, magnetism, conductivity, and magnetoelectric coupling of the ordered nanocomposites were characterized by scanning probe microscopy. The insulating $BiFeO_3$ matrix exhibited ferroelectric domains, whereas the resistive $CoFe_2O_4$ pillars exhibited single-domain magnetic contrast with high anisotropy due to the magnetoelasticity of the spinel phase. Magnetoelectric coupling was observed in which an applied voltage led to reversal of the magnetic pillars.

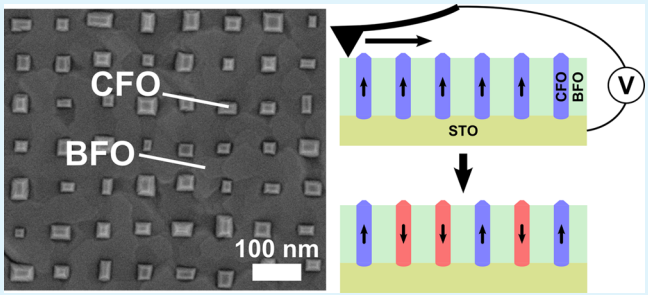

KEYWORDS: *magnetoelectric coupling, templated self-assembly, vertically aligned nanocomposites, piezo-response force microscopy, magnetic force microscopy, conductive AFM*

INTRODUCTION

Recent advances in the characterization of the magnetoelectric coupling in heterostructures comprised of a ferroelectric material and a ferro- or ferrimagnet have paved the way toward future devices based on the control of magnetization with an electric field.[1,2] Of particular interest are perovskite-spinel vertically aligned nanocomposites, such as $BaTiO_3$–$CoFe_2O_4$,[3] which self-assemble into a pillar-matrix nanostructure upon codeposition of the immiscible component phases. These so-called 1–3 multiferroic nanocomposites can exhibit a higher magnetoelectric coupling than their laminate counterparts because of the higher interfacial area between the two phases and the reduced clamping constraints from the substrate.[4] A wide range of other component materials have been demonstrated, such as $BiFeO_3$[5] or $PbTiO_3$[6] for the perovskite matrix and $NiFe_2O_4$[7] or $MgFe_2O_4$[8] for the spinel pillars. Intermediate compositions such as $Co_xMg_{1-x}Fe_2O_4$[9] and $Co_xNi_{1-x}Fe_2O_4$[10] have also been achieved thanks to recent advances in deposition methods.[11]

In $BiFeO_3$–$CoFe_2O_4$ (BFO/CFO) nanocomposites, the electrically assisted magnetic switching of ferrimagnetic pillars was demonstrated experimentally[12] for a collection of pillars and studied theoretically[13] at the scale of a single pillar, which further highlighted these materials as promising for electrically switchable devices. However, without additional processing steps, the magnetic pillars have a range of diameters and are randomly located, making the nanocomposites unsuitable for most device applications. Recent efforts have thus been focused on achieving long-range order in the nanocomposite by directed self-assembly methods. This was realized previously by prepatterning a thin CFO layer into small seeds in controlled locations on the $SrTiO_3$ substrate, either by ion milling[14] or lift-off,[15] which then guided the growth of the composite. In those previous articles, the magnetic characterization of the templated nanocomposites was limited to measurements at remanence, and magnetoelectric coupling was only measured macroscopically.

In an earlier publication,[10] we presented a general method to template the self-assembly of perovskite/spinel nanocomposites, relying on topographical features written in the substrate which nucleated the growth of the nanopillars. By eliminating the need to directly pattern one of the constituents of the film, this selective nucleation-based method simplifies the templating process and reduces the risk of contamination and defects. High aspect ratio CFO nanostructures with sub-100 nm spacings were grown using this process, and their microstructure was analyzed. To understand the interplay between the fabrication method and material properties and to study how the templating process affects the strain-mediated magnetoelectric coupling of BFO–CFO nanostructures, we use scanning probe microscopy-based techniques to characterize their electrical and magnetic behavior.

RESULTS AND DISCUSSION

The square arrays of CFO pillars had periods between 67 and 100 nm and covered areas of a few sqare micrometers. The film

Received: September 11, 2014
Accepted: January 5, 2015
Published: January 5, 2015

DOI: 10.1021/am506089c
ACS Appl. Mater. Interfaces 2015, 7, 2263–2268

thicknesses were between 50 and 100 nm. Figure 1a shows a top-view scanning electron microscopy (SEM) image of a

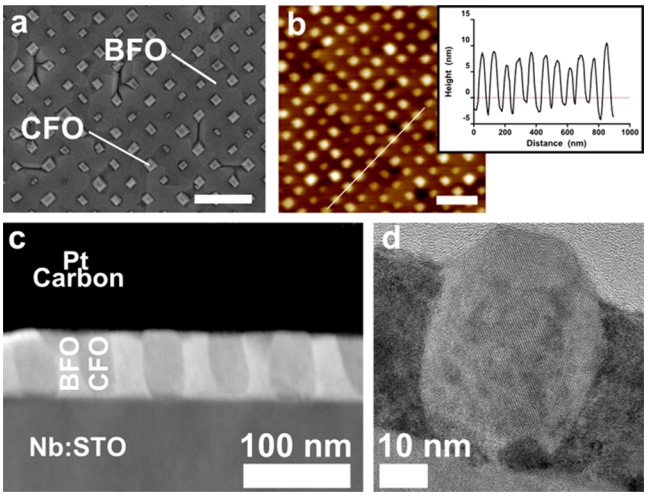

Figure 1. (a) Top-view SEM image of a BFO−CFO nanocomposite templated into a square array with period 80 nm, in which the CFO pillars show as bright regions (scale bar: 100 nm). (b) AFM topography image taken on the same sample, with the inset showing a line profile along a row of pillars (scale bar: 100 nm). (c) HAADF TEM cross-section of a sample with period 100 nm. (d) HRTEM close-up image around a CFO pillar.

square array with period 83 nm. The bright rectangular islands visible in this image correspond to the (111)-faceted tops of the CFO pillars, while the darker area corresponds to the single-crystal BFO matrix. The surface topography measured by atomic force microscopy (AFM), which is shown in Figure 1b, reveals that the CFO pillars protrude by 10−15 nm above the BFO matrix. The BFO grows following a Stranski−Krastanov mode on STO,[16] naturally forming faceted structures after the growth of a few monolayers to relieve the epitaxial strain originating from the substrate. In our templated samples, the additional presence of templated CFO pillars promotes faceting in specific locations between two pillars, as seen in Figure 1a, to relieve some of the additional strain due to the vertical interfaces. The lattice parameters for bulk BFO and bulk CFO are 3.96 Å and (2 × 4.18) Å, respectively, representing a large mismatch of 5.5%. In contrast with the epitaxial strain due to the substrate, the BFO−CFO mismatch along the vertical interfaces represents an additional energy term maintained throughout the film thickness,[17] in the form of either elastic energy or of interfacial energy if dislocations are created.

The high-angle annular dark field transmission electron microscopy (HAADF TEM) image in Figure 1c clearly shows the columnar structure with CFO pillars appearing darker than the BFO matrix because they contain elements of lower atomic number. The TEM lamella prepared by focused ion beam (FIB) was thick enough to include two rows of CFO pillars, separated by $\sqrt{2}/2$ times the period of the square lattice. A high-resolution TEM (HRTEM) image is shown in Figure 1d, taken along the [110] zone axis, in which the lattice fringes can be seen corresponding to the substrate and the two phases within the film, confirming the cube-on-cube epitaxy. Lattice parameters were measured from fast fourier transform images from the three phases. Strain relaxation in the thin TEM lamella prevented an accurate determination of the original strain state of the film, but it agreed qualitatively with the strain found in untemplated BFO/CFO self-assembled nanocomposites by X-ray diffraction,[11] in which the BFO was in out-of-plane tension (around 4.04 Å out-of-plane lattice parameter) and the CFO in out-of-plane compression. The vertical interfaces between the BFO and the CFO are semicoherent, with misfit dislocations present according to TEM (not shown).

Conductive AFM (cAFM) characterization was performed, as shown in Figure 2a, for an applied sample bias of 3 V. When

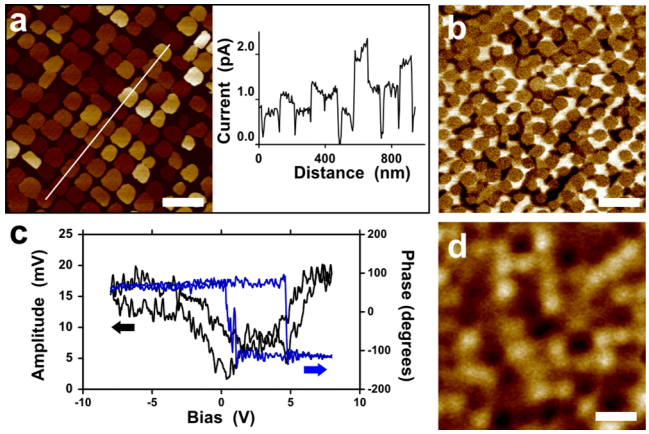

Figure 2. (a) cAFM image taken on a BFO−CFO sample templated with period 100 nm (left) and conduction profile along a row of CFO pillars (right). (b) PFM image on the same sample. (c) PFM amplitude and phase as a function of DC bias voltage, at a location corresponding to the BFO. (d) MFM image after AC demagnetization. All scale bars represent 200 nm.

the conductive probe was in contact with the BFO only, the current was below the sensitivity limit of the instrument, which is around 100 fA. On the contrary, when the probe touched a CFO pillar, a current ranging from around 0.5 to 2.5 pA could be measured, with remarkable homogeneity throughout the area of each pillar. This flat conductivity profile is unlikely to originate from topographic contribution to the cAFM signal since the pyramidal CFO islands exhibit sharp edges (the topography AFM images corresponding to Figure 2a, b, and d are available in the Supporting Information). Unlike previous cAFM studies on BFO−CFO nanocomposites,[18] where nA-range currents were measured at the interface between the two phases, no interfacial high conductivity path was seen in our experiments. This could indicate that the vertical interfaces in our samples contain a lower concentration of defects, inhibiting the mobility of oxygen vacancies.[19,20] From our measurements, the resistivity of the CFO can be estimated at $\rho = (U/I)(A/L) = 2 \times 10^6$ Ω·cm, where U is the applied bias in volts, I the measured current in amperes, A the average area of a CFO pillar in cm^2, and L its average length in cm. This value of the resistivity is in agreement with values reported in the literature for CFO, which range from 10^5 to 10^7 Ω·cm.[21,22] On the other hand, the value of the resistivity for BFO is expected to be close to 10^{10} Ω.cm,[23] which explains why no current could be sensed passing through the matrix. This insulating character is a requirement for the ferroelectric behavior described below.

Piezoresponse force microscopy (PFM) measurements confirmed the ferroelectric nature of the BFO. Figure 2b shows a PFM image taken on a templated sample with a square lattice of period 83 nm and a film thickness of 100 nm. The areas where contrast can be observed in the piezoresponse corresponded to the BFO matrix, whereas no signal could be

DOI: 10.1021/am506089c
ACS Appl. Mater. Interfaces 2015, 7, 2263−2268

measured on the CFO pillars. Ferroelectric domains are clearly visible, which appear as bright and dark patches corresponding to their respective out-of-plane polarization components. Because the BFO is expected to be in its rhombohedral phase, based on XRD data acquired on untemplated composites grown in the same deposition conditions (see the Supporting Information), the polarization of the ferroelectric domains is expected to be along the pseudocubic <111> directions which are oriented at 55° from the substrate normal. Consequently, the dark (bright) domains in the PFM image can be any of the four variants pointing up (down). The ferroelectric switching of the BFO matrix was studied by measuring local hysteresis loops of the PFM amplitude and phase as a function of voltage, as shown in Figure 2c. A clear hysteresis can be observed in the phase data, with saturation values separated by 180°. The amplitude data have a typical butterfly shape, with minima corresponding to the switching voltages in the phase data. A coercive field of about 200 kV·cm^{-1} (2 V over 100 nm) was measured, which is in good agreement with reported values for pulsed laser deposition (PLD)-deposited BFO.[15,24] The horizontal offset of the hysteresis loop, which varied spatially over the BFO phase and indicates a local preferred direction of the polarization, is commonly observed in ferroelectric thin films, and its origin is still the subject of debate.[25,26]

Figure 2d shows a magnetic force microscopy (MFM) image taken on a similar sample with thickness 100 nm. The MFM measurement was done after an ac-demagnetization in the out-of-plane direction. A one to one correspondence can be observed between the topographical location of the pillars and areas of bright and dark contrast in the MFM image, consistent with an out-of-plane single domain magnetization of the pillars. The random distribution of up-magnetized and down-magnetized pillars indicates that magnetostatic interactions played a very limited role in determining the magnetic ground state of the array. Indeed, strong magnetostatic interactions would result in local checkerboard-like patterns of up- and down-magnetized pillars after ac-demagnetization.[27−29] Using a dipolar-interaction model with interpillar spacing of 80 nm, film thickness of 60 nm, and lateral pillar diameter of 40 nm, the nearest-neighbor magnetostatic interaction field is given by $H_i = M_s(v/p^3) = 75$ Oe, where $M_s = 400$ emu·cm^{-3} is the saturation magnetization of CFO,[11] v the volume of the pillars, and p the period of the array. The net magnetostatic interaction field is at most $9H_i = 680$ Oe in a square array, which as we will see below is small compared to the average pillar switching field.

A remanence curve of the templated pillars was produced by taking MFM images after applying different reversal fields ex situ using the electromagnet of a vibrating sample magnetometer (VSM). The magnetization of the samples was initially saturated with a large negative out-of-plane magnetic field of amplitude 12.5 kOe. Then a series of positive fields were applied with increasing amplitude, and the MFM image of the same templated region was acquired at remanence after each positive field. The corresponding images are shown in Figure 3a for a square array with period 80 nm.

To identify the magnetic switching of individual CFO pillars, difference images were calculated between successive MFM images to emphasize the regions where the magnetization was changed. Because there were variations in the sample drift during the acquisition of the MFM images, these deformations had to be taken into account when subtracting one image from another. Affine transformations were used to compensate for

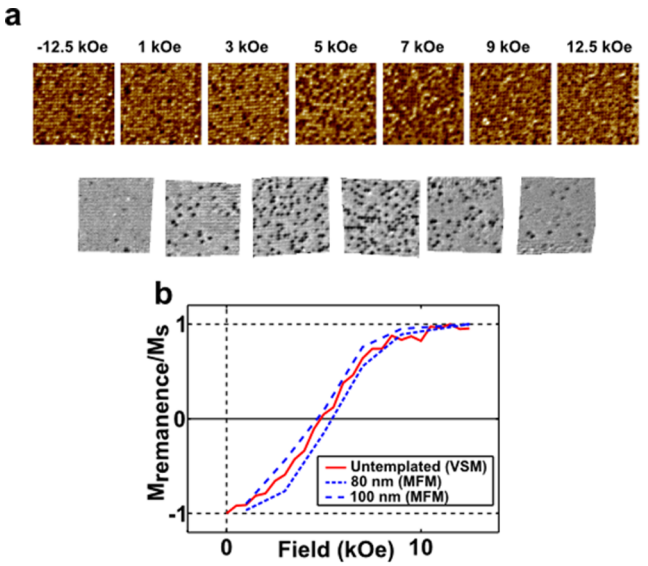

Figure 3. (a) Series of 2 × 2 μm^2 MFM images taken on BFO−CFO templated nanocomposites at remanence after the application of increasing magnetic fields (top) and the corresponding calculated difference images (bottom). (b) Remanence curve measured from the MFM data for templated nanocomposites with periods 80 and 100 nm and by VSM for an untemplated sample.

differences in drift between the successive images.[30] The Matlab code employed for treating the raw data is described in detail in the Supporting Information. The resulting processed images are shown in the lower part of Figure 3a and reveal that most CFO pillars reversed their magnetization at fields between 3 and 9 kOe.

To extract the value of the remanent coercivity, the MFM remanence curves were constructed by first counting the number of switching events in each difference image. This was done algorithmically by image processing and particle counting. The MFM remanence curve was calculated from the cumulative sums of the magnetic switching events as a function of field. This method assumes that each pillar switching event contributed equally to the total magnetic reversal of the sample. The validity of these assumptions is discussed in more length in the Supporting Information.

The resulting remanence curves are shown in Figure 3b for templated arrays with period of 80 and 100 nm, along with a remanence curve measured using a VSM on an untemplated nanocomposite deposited under the same conditions and with the same 60 nm thickness. The untemplated sample had an average pillar spacing of about 60 nm, with a wider spread of pillar diameters between 30 and 100 nm. The shape of the curve and coercive field were very similar in the templated and untemplated cases, revealing that the templating of the pillars had little influence on the magnetic properties of the composite. In particular, the remanent coercivity, which is a good estimate of the average switching field of the pillars, was around 5 kOe in all cases. This value is much higher than the estimated magnetostatic interaction fields which explains why magnetostatic interactions had a negligible effect on the reversal process of the pillars. The wide switching field distribution is attributed to a distribution in pillar geometries and/or strain states.

The coercivity of the pillars was higher than expected from shape anisotropy (which would be around 2.5 kOe based on

DOI: 10.1021/am506089c
ACS Appl. Mater. Interfaces 2015, 7, 2263−2268

coherent rotation) and indicates the contribution of an additional anisotropy, which we attribute to magnetoelastic anisotropy. The compressive out-of-plane strain of the CFO phase, measured by XRD on the untemplated sample of Figure 3, was −0.19% (see the Supporting Information), which, combined with the reported magnetostrictive coefficients of CFO between[3,31,32] $\lambda_{100} = -350 \times 10^{-6}$ and -590×10^{-6}, yields a switching field between 7.85 and 11.5 kOe[11] under the coherent rotation assumption, including the shape anisotropy contribution. The remanent coercivity of 5 kOe is smaller than these estimates, which could indicate an incoherent reversal process.

The effect of exchange coupling between the BFO (which is antiferromagnetic) and the CFO was explored by field-cooling the samples, but it had no significant effects on the reversal process because the exchange coupling in BFO/ferrimagnetic spinel composites is nonexistent[29,33] or weak (100 Oe or less[34,35]) in BFO-based all-oxide systems at room temperature.

Magnetoelectric coupling between the ferroelectricity of the BFO matrix and the magnetization of the CFO pillars was studied by comparing MFM images of the same templated region before and after doing a PFM measurement on a 2 × 2 μm^2 area. A 3 × 3 μm^2 AFM image of the area of interest is shown in Figure 4a. The 3 × 3 μm^2 MFM images are shown in Figure 4b and c. The sample was initially imaged by MFM at remanence after the application of a strong out-of-plane magnetic field and then imaged again after taking a PFM scan to see whether the ferroelectric switching led to any change in the magnetization of the CFO pillars in the absence of a magnetic field.

A nonmagnetic probe was used for the PFM imaging, which was carried out at an applied AC voltage of 3 V within the 2 × 2 μm^2 area. The use of a nonmagnetic tip for PFM imaging avoided changes in magnetization due to the stray field of the tip such as that shown in Figure 4b, in which a tip-induced magnetization reversal (a sudden change of contrast from bright to dark from one scanned line to the next) is indicated with a circle. To visualize the magnetization switching induced by PFM imaging, the same algorithm was used as in Figure 3 to correct for the slight image deformations and obtain a difference image. The result is shown in Figure 4d, in which the area measured by PFM is also indicated. The regions of highest contrast mostly matched the PFM area, with bright and dark patches corresponding to the magnetization reversal of pillars. The presence of both dark and light contrast in the difference image indicates that pillars switched from up to down and from down to up magnetization during the PFM scanning. Isolated reversal events can also be seen outside of the area that underwent PFM, but these all showed as dark contrast and could therefore be due to the effect of the field from the magnetic probe tip.

Magnetization reversal could also be a result of the Joule heating caused by the flow of current through the nanopillars because a temperature increase can lower the magnetic anisotropy. The power dissipation was on the order of 1 pW (of order 1pA × 1 V) per pillar, i.e., 10^{10} W·m^{-3}. Solving the heat equation for a homogeneous source of radius r_0 dissipating heat Q inside an infinite medium, with boundaries at a fixed temperature, yields a rise of temperature of the source on the order of $(Qr_0^2)/\kappa$ at the steady state. κ is the thermal conductivity of the surrounding medium, taken to be that of STO for simplicity, i.e., κ = 10 W·m^{-1}·K^{-1}.[36] For a source of the size of the pillars, r_0 is around 30 nm, giving a temperature

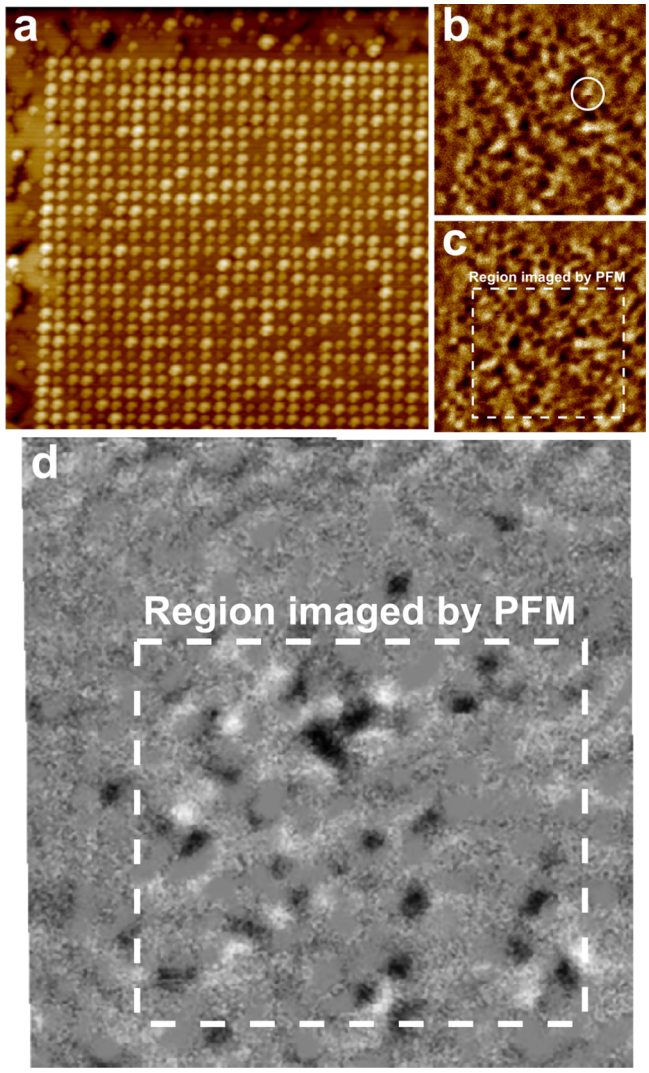

Figure 4. (a) 3 × 3 μm^2 AFM image of a templated area with period 100 nm, where the magnetoelectric coupling was measured. (b) and (c) MFM images, respectively, taken before and after taking a PFM image in a smaller 2 × 2 μm^2 area. (d) Difference MFM image calculated from (b) and (c).

increase on the order of 10^{-4} K. This is negligible and indicates that Joule heating is not responsible for the magnetization switching.

Magnetization reversal is therefore most likely due to magnetoelectric coupling of the CFO with the ferroelectric BFO. One possible coupling mechanism between BFO and CFO is via exchange coupling between uncompensated interface spins in the antiferromagnetic BFO and the magnetization in the CFO. In the BFO, the antiferromagnetism is coupled to the ferroelectric domains and can be affected by an electric field, as observed elsewhere.[32,37] However, our measurements showed no evidence for this mechanism such as enhanced anisotropy, exchange bias, or saturation magnetization. Instead, as observed previously in untemplated samples,[12] the reversal of magnetization is attributed to an anisotropy change induced by strain transferred from the ferroelectric BFO as it undergoes electrostriction. The voltage of amplitude 3 V ac (at 3 kHz) applied during PFM imaging, over a film thickness of 60 nm, gives an electric field magnitude that is similar to the 16 V dc over 300 nm used by Zavaliche et

DOI: 10.1021/am506089c
ACS Appl. Mater. Interfaces 2015, 7, 2263−2268

al.,[12] further supporting the mechanism of strain-mediated magnetoelectric coupling. In this scenario, the deformations experienced by the BFO under the ac voltage, which exist with or without ferroelectric switching, cycle the strain state of the CFO pillars, which could lower their anisotropy sufficiently to allow switching from the stray fields of their neighbors. Further studies of the influence of an applied voltage on the shape of the remanence magnetization curve, measured locally using the MFM method described in this work, would yield valuable information on the mechanism of magnetoelectric coupling.

CONCLUSION

In conclusion, templated BFO−CFO nanocomposites, in which the CFO pillars were patterned into square arrays with periods between 60 and 100 nm, showed ferroelectric, ferrimagnetic, and magnetoelectric properties. The BFO matrix was ferroelectric and insulating, with a clear domain structure with domain sizes on the order of the pillar period and a coercive field of 200 kV·cm^{-1}. The magnetic switching field of the CFO pillars was measured from the remanence curve derived from MFM measurements, yielding a remanent coercivity of around 5 kOe. The remanent curves of templated and untemplated nanocomposites were similar, which indicated that magnetostatic interactions between pillars had a minor effect of the switching of the array. This is explained by the dominance of the magnetoelastic anisotropy contribution in $CoFe_2O_4$ pillars, such that their switching field is much greater than the magnetic field from nearest-neighbor pillars. Magnetoelectric coupling was observed by applying an ac voltage to the BFO matrix, which caused the reversal of magnetization in some of the CFO pillars.

The possibility to template the nanocomposite into useful structures without compromising the magnetic, ferroelectric, and magnetoelectric properties is promising for the development of multiferroic memory or logic devices in which local electric fields promote reversal of specific magnetic pillars.[38] Furthermore, by adjusting the composition of the pillars[10] the magnetoelastic anisotropy can be controlled or reduced to the extent that magnetostatic interactions become important at sub-100 nm periods, enabling studies of magnetic frustration in hexagonal arrays and the design of magnetic quantum cellular automata devices using these nanocomposites. Finally, our work demonstrates that templated self-assembly is a viable processing path for devices leveraging the novel interfacial and strain-related properties exhibited by vertically aligned oxide nanocomposites.

METHODS

The BFO−CFO nanocomposites were grown by pulsed laser deposition (PLD), at a wavelength of 248 nm and a fluence of around 2 J·cm^{-2}, from two different targets of compositions $Bi_{1.2}FeO_3$ and $CoFe_2O_4$. The O_2 partial pressure was 5 mTorr, and the substrate temperature was between 580 and 650 °C. The substrates were (001) Nb-doped $SrTiO_3$ (Nb:STO) substrates patterned using a focused ion beam (FIB). Topographical pits were patterned in the substrate which induced the selective nucleation of the CFO phase and provided control over the final morphology of the nanostructure. Details of the fabrication method are described elsewhere,[10] along with a discussion on the processes responsible for the templated self-assembly. Scanning electron microscopy images were taken with a Helios 600 dual-beam microscope, and transmission electron microscopy was carried out using a JEOL 2010F Field emission TEM. Atomic force microscopy (AFM), conductive AFM (cAFM), piezoresponse force microscopy (PFM), and magnetic force microscopy (MFM) measurements were performed on a Veeco Metrology Nanoscope V Scanned Probe Microscope with Dimension 3100 SPM (LS) equipped with a tunneling AFM (TUNA) module, using MicroMasch HQ:NSC19/CR-Au (tip radius < 30 nm) and Bruker MESP-RC probes (tip radius <50 nm).

ASSOCIATED CONTENT

Supporting Information

X-ray diffraction measurements on untemplated samples, topographic AFM images corresponding to the cAFM, PFM, and MFM measurements, and cAFM $I-V$ curves across the CFO−BFO interface. A description of the MFM-based measurement of the magnetic remanence curve and the corresponding Matlab code are also provided. This material is available free of charge via the Internet at http://pubs.acs.org.

AUTHOR INFORMATION

Corresponding Authors

*E-mail: naimo@mit.edu
*E-mail: caross@mit.edu.

Notes

The authors declare no competing financial interest.

ACKNOWLEDGMENTS

The support of the National Science Foundation and FAME, one of six centers of STARnet, a Semiconductor Research Corporation program sponsored by MARCO and DARPA, is acknowledged. Shared experimental facilities of CMSE, award NSF0819762, were used. The authors thank Youssef Mroueh for his help on the image processing.

REFERENCES

(1) Vaz, C. A. F. Electric Field Control of Magnetism in Multiferroic Heterostructures. *J. Phys.: Condens. Matter* **2012**, *24*, 333201.
(2) Nan, C.-W.; Bichurin, M. I.; Dong, S.; Viehland, D.; Srinivasan, G. Multiferroic Magnetoelectric Composites: Historical Perspective, Status, and Future Directions. *J. Appl. Phys.* **2008**, *103*, 031101.
(3) Zheng, H.; et al. Multiferroic $BaTiO_3$-$CoFe_2O_4$ Nanostructures. *Science* **2004**, *303*, 661−3.
(4) Schmitz-Antoniak, C.; Schmitz, D.; Borisov, P.; de Groot, F. M. F.; Stienen, S.; Warland, A.; Krumme, B.; Feyerherm, R.; Dudzik, E.; Kleemann, W.; Wende, H. Electric In-plane Polarization in Multiferroic $CoFe_2O_4$/$BaTiO_3$ Nanocomposite Tuned by Magnetic Fields. *Nat. Commun.* **2013**, *4*, 2051.
(5) Zheng, H.; Straub, F.; Zhan, Q.; Yang, P.-L.; Hsieh, W.-K.; Zavaliche, F.; Chu, Y.-H.; Dahmen, U.; Ramesh, R. Self-Assembled Growth of $BiFeO_3$-$CoFe2O_4$ Nanostructures. *Adv. Mater.* **2006**, *18*, 2747−2752.
(6) Levin, I.; Li, J.; Slutsker, J.; Roytburd, A. L. Design of Self-Assembled Multiferroic Nanostructures in Epitaxial Films. *Adv. Mater.* **2006**, *18*, 2044−2047.
(7) Zhan, Q.; Yu, R.; Crane, S. P.; Zheng, H.; Kisielowski, C.; Ramesh, R. Structure and Interface Chemistry of Perovskite-Spinel Nanocomposite Thin Films. *Appl. Phys. Lett.* **2006**, *89*, 172902.
(8) Kim, D. H.; Aimon, N. M.; Ross, C. A. Self-Assembled Growth and Magnetic Properties of a $BiFeO_3$-$MgFe_2O_4$ Nanocomposite Prepared by Pulsed Laser Deposition. *J. Appl. Phys.* **2013**, *113*, 17B510.
(9) Kim, D. H.; Aimon, N. M.; Sun, X.; Ross, C. A. Compositionally Modulated Magnetic Epitaxial Spinel/Perovskite Nanocomposite Thin Films. *Adv. Funct. Mater.* **2013**, 3063−3067.
(10) Aimon, N. M.; Choi, H. K.; Sun, X. Y.; Kim, D. H.; Ross, C. A. Templated Self-Assembly of Functional Oxide Nanocomposites. *Adv. Mater.* **2014**, *26*, 3063−3067.
(11) Aimon, N. M.; HunKim, D.; KyoonChoi, H.; Ross, C. A. Deposition of Epitaxial $BiFeO_3$/$CoFe_2O_4$ Nanocomposites on (001)

DOI: 10.1021/am506089c
ACS Appl. Mater. Interfaces 2015, 7, 2263−2268

$SrTiO_3$ by Combinatorial Pulsed Laser Deposition. *Appl. Phys. Lett.* **2012**, *100*, 092901.
(12) Zavaliche, F.; Zhao, T.; Zheng, H.; Straub, F.; Cruz, M. P.; Yang, P.-L.; Hao, D.; Ramesh, R. Electrically Assisted Magnetic Recording in Multiferroic Nanostructures. *Nano Lett.* **2007**, *7*, 1586−90.
(13) Aimon, N. M.; Liao, J.; Ross, C. A. Simulation of Inhomogeneous Magnetoelastic Anisotropy in Ferroelectric/Ferromagnetic Nanocomposites. *Appl. Phys. Lett.* **2012**, *101*, 232901.
(14) Comes, R.; Liu, H.; Khokhlov, M.; Kasica, R.; Lu, J.; Wolf, S. A. Directed Self-Assembly of Epitaxial $CoFe_2O_4$-$BiFeO_3$ Multiferroic Nanocomposites. *Nano Lett.* **2012**, *12*, 2367−73.
(15) Stratulat, S. M.; Lu, X.; Morelli, A.; Hesse, D.; Erfurth, W.; Alexe, M. Nucleation-Induced Self-Assembly of Multiferroic $BiFeO_3$-$CoFe_2O_4$ Nanocomposites. *Nano Lett.* **2013**, *13*, 3884−9.
(16) Chinta, P. V.; Callori, S. J.; Dawber, M.; Ashrafi, A.; Headrick, R. L. Transition from Laminar to Three-Dimensional Growth Mode in Pulsed Laser Deposited $BiFeO_3$ Film on (001) $SrTiO_3$. *Appl. Phys. Lett.* **2012**, *101*, 201602.
(17) Chen, A.; Weigand, M.; Bi, Z.; Zhang, W.; Lü, X.; Dowden, P.; MacManus-Driscoll, J. L.; Wang, H.; Jia, Q. Evolution of Microstructure, Strain and Physical Properties in Oxide Nanocomposite Films. *Sci. Rep* **2014**, *4*, 5426.
(18) Hsieh, Y.-H.; Liou, J.-M.; Huang, B.-C.; Liang, C.-W.; He, Q.; Zhan, Q.; Chiu, Y.-P.; Chen, Y.-C.; Chu, Y.-H. Local Conduction at the BiFeO(3)-CoFe(2)O(4) Tubular Oxide Interface. *Adv. Mater.* **2012**, *24*, 4564−8.
(19) Hsieh, Y.-H.; Strelcov, E.; Liou, J.-M.; Shen, C.-Y.; Chen, Y.-C.; Kalinin, S. V.; Chu, Y.-H. Electrical Modulation of the Local Conduction at Oxide Tubular Interfaces. *ACS Nano* **2013**, *7*, 8627−33.
(20) Strelcov, E.; Belianinov, A.; Hsieh, Y.-H.; Jesse, S.; Baddorf, A. P.; Chu, Y.-H.; Kalinin, S. V. Deep Data Analysis of Conductive Phenomena on Complex Oxide Interfaces: Physics from Data Mining. *ACS Nano* **2014**, *8*, 6449−57.
(21) Thang, P.; Rijnders, G.; Blank, D. Stress-Induced Magnetic Anisotropy of $CoFe_2O_4$ Thin Films Using Pulsed Laser Deposition. *J. Magn. Magn. Mater.* **2007**, *310*, 2621−2623.
(22) Goldman, A. *Modern Ferrite Technology*; Springer: U.S., 2006.
(23) Catalan, G.; Scott, J. F. Physics and Applications of Bismuth Ferrite. *Adv. Mater.* **2009**, *21*, 2463−2485.
(24) Wang, J.; Neaton, J. B.; Zheng, H.; Nagarajan, V.; Ogale, S. B.; Liu, B.; Viehland, D.; Vaithyanathan, V.; Schlom, D. G.; Waghmare, U. V.; Spaldin, N. A.; Rabe, K. M.; Wuttig, M.; Ramesh, R. Epitaxial $BiFeO_3$ Multiferroic Thin Film Heterostructures. *Science* **2003**, *299*, 1719−22.
(25) Caruntu, G.; Yourdkhani, A.; Vopsaroiu, M.; Srinivasan, G. Probing the Local Strain-Mediated Magnetoelectric Coupling in Multiferroic Nanocomposites by Magnetic Field-Assisted Piezoresponse Force Microscopy. *Nanoscale* **2012**, *4*, 3218−27.
(26) Folkman, C. M.; Baek, S. H.; Nelson, C. T.; Jang, H. W.; Tybell, T.; Pan, X. Q.; Eom, C. B. Study of Defect-Dipoles in an Epitaxial Ferroelectric Thin Film. *Appl. Phys. Lett.* **2010**, *96*, 052903.
(27) Hwang, M.; Abraham, M. C.; Savas, T. A.; Smith, H. I.; Ram, R. J.; Ross, C. A. Magnetic Force Microscopy Study of Interactions in 100 nm Period Nanomagnet Arrays. *J. Appl. Phys.* **2000**, *87*, 5108.
(28) Ross, C.; Hwang, M.; Shima, M.; Cheng, J.; Farhoud, M.; Savas, T.; Smith, H.; Schwarzacher, W.; Ross, F.; Redjdal, M.; Humphrey, F. Micromagnetic Behavior of Electrodeposited Cylinder Arrays. *Phys. Rev. B* **2002**, *65*, 144417.
(29) Bromwich, T. J.; Kasama, T.; Chong, R. K. K.; Dunin-Borkowski, R. E.; Petford-Long, a. K.; Heinonen, O. G.; Ross, C. A. Remanent Magnetic States and Interactions in Nano-Pillars. *Nanotechnology* **2006**, *17*, 4367−4373.
(30) Czoschke, P.; Nazarov, A. V.; McKinlay, S. E.; Singleton, E. W.; Pant, B. B. Imaging of Isolated Magnetic Cluster Switching in Thin CoCrPt Films. *J. Appl. Phys.* **2008**, *103*, 07D916.
(31) Bozorth, R.; Tilden, E.; Williams, A. Anisotropy and Magnetostriction of Some Ferrites. *Phys. Rev.* **1955**, *99*, 1788−1798.
(32) Zhang, W.; Jian, J.; Chen, A.; Jiao, L.; Khatkhatay, F.; Li, L.; Chu, F.; Jia, Q.; MacManus-Driscoll, J. L.; Wang, H. Strain Relaxation and Enhanced Perpendicular Magnetic Anisotropy in Bi-FeO_3:$CoFe_2O_4$ Vertically Aligned Nanocomposite Thin Films. *Appl. Phys. Lett.* **2014**, *104*, 062402.
(33) Sun, M. Y.; Li, P.; Jin, C.; Wang, L. Y.; Zheng, D. X.; Bai, H. L. Enhanced Exchange Bias in Fully Epitaxial Fe3O4/Tetragonal-like BiFeO3Magnetoelectric Bilayers. *Europhys. Lett.* **2014**, *105*, 17007.
(34) Qi, X.; Kim, H.; Blamire, M. G. Exchange Bias in Bilayers Based on the Ferroelectric Antiferromagnet BiFeO3. *Philos. Mag. Lett.* **2007**, *87*, 175−181.
(35) Yang, C.-H.; Yildiz, F.; Lee, S.-H.; Jeong, Y. H.; Chon, U.; Koo, T. Y. Synthesis of Nanoscale Composites of Exchange Biased MnFe2O4 and Mn-doped BiFeO3. *Appl. Phys. Lett.* **2007**, *90*, 163116.
(36) Kim, Y.; Kumar, A.; Tselev, A.; Kravchenko, I. I.; Han, H.; Vrejoiu, I.; Lee, W.; Hesse, D.; Alexe, M.; Kalinin, S. V.; Jesse, S. Nonlinear Phenomena in Multiferroic Manocapacitors: Joule Heating and Electromechanical Effects. *ACS Nano* **2011**, *5*, 9104−12.
(37) Chen, Y.-J.; Hsieh, Y.-H.; Liao, S.-C.; Hu, Z.; Huang, M.-J.; Kuo, W.-C.; Chin, Y.-Y.; Uen, T.-M.; Juang, J.-Y.; Lai, C.-H.; Lin, H.-J.; Chen, C.-T.; Chu, Y.-H. Strong Magnetic Enhancement in Self-Assembled Multiferroic-Ferrimagnetic Nanostructures. *Nanoscale* **2013**, *5*, 4449−53.
(38) Kabir, M.; Stan, M. R.; Wolf, S. A.; Comes, R. B.; Lu, J. RAMA: a Self-Assembled Multiferroic Magnetic QCA for Low Power Systems. *ACM Great Lakes Symposium on VLSI'11*; 2011; p 25.

DOI: 10.1021/am506089c
ACS Appl. Mater. Interfaces 2015, 7, 2263−2268